Journal of Alloys and Compounds 791 (2019) 1005–1014

Contents lists available at ScienceDirect

Journal of Alloys and Compounds

journal homepage: http://www.elsevier.com/locate/jalcom

Design and synthesis of phosphomolybdic acid/silver dual-modified microporous carbon composite for high performance supercapacitors

Chen Jiao [a, b], Ji Lian Xu [a, *], Xiang Ying Chen [d], Zhong Jie Zhang [c, **]

[a] State Key Laboratory of Luminescence and Applications Changchun Institute of Optics, Fine Mechanics and Physics Chinese Academy of Sciences, No. 3888 Dongnanhu Road, Changchun 130033, PR China
[b] University of Chinese Academy of Sciences, Beijing 100049, PR China
[c] School of Chemistry & Chemical Engineering, Anhui Province Key Laboratory of Environment-friendly Polymer Materials, Anhui University, Hefei 230601, Anhui, PR China
[d] School of Chemistry and Chemical Engineering, Anhui Key Laboratory of Controllable Chemistry Reaction & Material Chemical Engineering, Hefei University of Technology, Hefei, Anhui 230009, PR China

ARTICLE INFO

Article history:
Received 27 January 2019
Received in revised form
27 February 2019
Accepted 27 March 2019
Available online 30 March 2019

Keywords:
Microporous carbon
Silver
Phosphomolybdic acid
Modification
Supercapacitor

ABSTRACT

We have developed a new energy system of microporous carbon/Ag/phosphomolybdic acid (PMA) as efficient electrode hybrid material for supercapacitors, in which microporous carbon serves as carbon support (contribution of EDLCs), PMA as redox additive (contribution of pseudocapacitance), Ag as conducting agent (promotion of electrical conductivity). It reveals that the dual incorporation of Ag and PMA leads to the large decrease of surface area and pore volume but the capacitive performance such as specific capacitance, rate capability and coulombic efficiency has remarkably improved due to the synergistic effect among the hybrid materials. For example, the energy density has reached up to 5.68 Wh kg^{-1} at the power density of 500 W kg^{-1}, which is almost 1.80 fold of pristine microporous carbon. Hybridizing polyoxometalate, carbon materials as well as conducting agent has provided an alternative electrode material for high performance supercapacitors.

1. Introduction

Carbon materials ranging from activated carbons to carbon nanotubes, graphene etc. are the most widely used electrode candidates owing to their advantageous properties including high surface area and pore volume, low cost, variety of form, inert electrochemistry, chemical stability in different solutions (from strongly acidic to basic) [1–4]. Especially for the case of activated carbon commonly possessing high surface area, it can provide an extensively large electrode/electrolyte interface for charge storage of supercapacitors, thus benefiting for producing more electric double-layer capacitances (EDLCs) [5]. Furthermore, another important factor that determines the performance of supercapacitors is electrical conductivity [6]. As reported previously, the electric conductivity of carbon materials is closely related to their morphology. The higher the surface area, the smaller the particle size, and the more poor the conductivity should be [7]. To further improve carbon's electrical conductivity, highly conductive substances such as silver nanoparticles [8], graphene/silver nanowires [9,10], and graphene-silver nanoparticles-polypyrrole nanocomposite [11] are usually introduced.

For the sake of achieving high energy density supercapacitors, apart from the contribution of EDLCs from carbon materials discussed above, another one from pseudocapacitances are also indispensable. The kind of pseudocapacitive contribution generally roots in metal oxides, conductive polymers, heteroatom-doping [12] as well as redox additives [13,14]. Alternatively, polyoxometalate (POM) clusters have emerged as intriguing candidates for energy storage systems as faradaic electrode materials and the most widely studied is the Keggin cluster [$MX_{12}O_{40}$], where M is the central heteroatom and X is the addenda atom (often as Mo, W or V) which forms a surrounding cage [15]. Interestingly, there exists a strong affinity between carbon matrix and POMs [16], making the hybridization of POMs and carbon materials more available. So far, many carbon-POMs composites have been developed, basically including single-walled carbon nanotubes (SWCNTs) with TBA-PV_2Mo_{10} [17], HT-RGO-PMo_{12} [18], activated

* Corresponding author.
** Corresponding author.
E-mail addresses: george13200@126.com (C. Jiao), xujl@ciomp.ac.cn (J.L. Xu), chenxy@hfut.edu.cn (X.Y. Chen), zhangzj06@ahu.edu.cn (Z.J. Zhang).

https://doi.org/10.1016/j.jallcom.2019.03.374
0925-8388/

carbon (AC)-PMo_{12} [19], biochar carbon-PMo_{12} [20], rGO-PMo_{12}-PW_{12} [21], micro-mesoporous carbon-PMo_{12} [22], AC-PW_{12} [23], rGO-PMoW [24], multi-walled carbon nanotubes (MWCNTs)-$PW_{12-x}Mo_x$ [25] and others [26–30]. Moreover, most of the deposition of POM molecules on carbon substrates has been realized by chemisorption technique, which is often described as strong and irreversible bonding [31]. Consequently, this tunability behavior of the POM oxidation and reduction states combined with the potential for multiple electron transfer provides many opportunities for engineering energy storage electrodes [15].

Herein, a new ternary energy system of PMA/Ag/microporous carbon as efficient electrode material for supercapacitors was designed, in which microporous carbon serves as carbon support (contribution of EDLCs), PMA as redox additive (contribution of pseudocapacitance), Ag as conducting agent (promotion of electrical conductivity). The microporous carbons dual-modified by PMA and/or Ag were characterized by a series of techniques such as Raman, Brunauer-Emmett-Teller (BET), X-ray photoelectron spectrum (XPS) to reveal the variation tendency of pristine structures, pore structures, and elemental species. Furthermore, the capacitive behaviors of the PMA/Ag/microporous carbon hybrid were tested in a three-electrode system and two-electrode system, respectively, mainly including cyclic voltammetry (CV), galvanostatic charge-discharge (GCD), Nyquist as well as the derivative specific capacitance, Ragone plot, coulombic efficiency, reaction kinetics.

2. Experimental section

All chemicals were purchased from Sinopharm Chemical Reagent Company, except for the AC materials from Nanjing XFNANO and used as received.

2.1. Typical procedure for synthesizing the carbon-Ag sample

The AC materials (1 g) was immersed into 25 mL $AgNO_3$ solution (*wt*, 15%) for 12 h at ambient condition, then filtered and dried at 110 °C for 6 h. Next, the above powder precursor was transferred into a porcelain boat. After flowing with N_2 for 30 min, it was further heated up to 600 °C at a rate of 4 °C min^{-1} and maintained for 2 h under N_2 flow in a horizontal tube furnace. After being cooled to room temperature, the ***carbon-Ag*** sample was obtained.

2.2. Typical procedure for synthesizing the carbon-Ag-PMA sample

The above ***carbon-Ag*** sample (0.5 g) was immersed into 25 mL PMA ($H_3PMo_{12}O_{40}$) solution (20 mmol L^{-1}) for 12 h at ambient condition, then filtered and dried at 110 °C for 6 h, obtaining the ***carbon-Ag-PMA*** sample. Note that there exists spontaneous and strong physic- and chemi-sorption between carbon and PMA, resulting in quick formation of ***carbon-Ag-PMA*** composite [32].

3. Results and discussion

3.1. Structural characterization

Towards the ***Carbon-blank, Carbon-Ag, Carbon-Ag-PMA*** samples, Raman spectra that are particularly sensitive to carbon microstructures were firstly employed to characterize their pristine structures together with the minor variation between them. Generally speaking, Raman spectrum for carbons is basically deconvoluted into D and G bands. But Sadezky et al. reported the first-order Raman bands and vibration modes for soot and graphite, in which five bands of G, D1 (D), D2 ($D^{/}$), D3 ($D^{//}$), and D4 (I) are presented within the wavenumber scope of 800–2000 cm^{-1} [33]. Fig. 1 indicates typical Raman spectra of the ***Carbon-blank, Carbon-Ag, Carbon-Ag-PMA*** samples when designating the wavenumber from 500 to 3500 cm^{-1}. With the help of Lorentzian fitting of multi-peaks, all of the present samples can be deconvoluted into four distinctive bands generally positioned at 1213, 1358, 1518, and 1622 cm^{-1}, respectively. In details, the peaks at 1358, and 1622 cm^{-1} are ascribed into D (A_{1g} symmetry) and G (E_{2g} symmetry) bands, respectively; the one at 1213 cm^{-1} attributes to disordered graphitic lattice and the one at 1518 cm^{-1} reveals the amorphous feature of carbons [33]. Apparently, these carbon samples qualitatively indicate amorphous nature with low degree

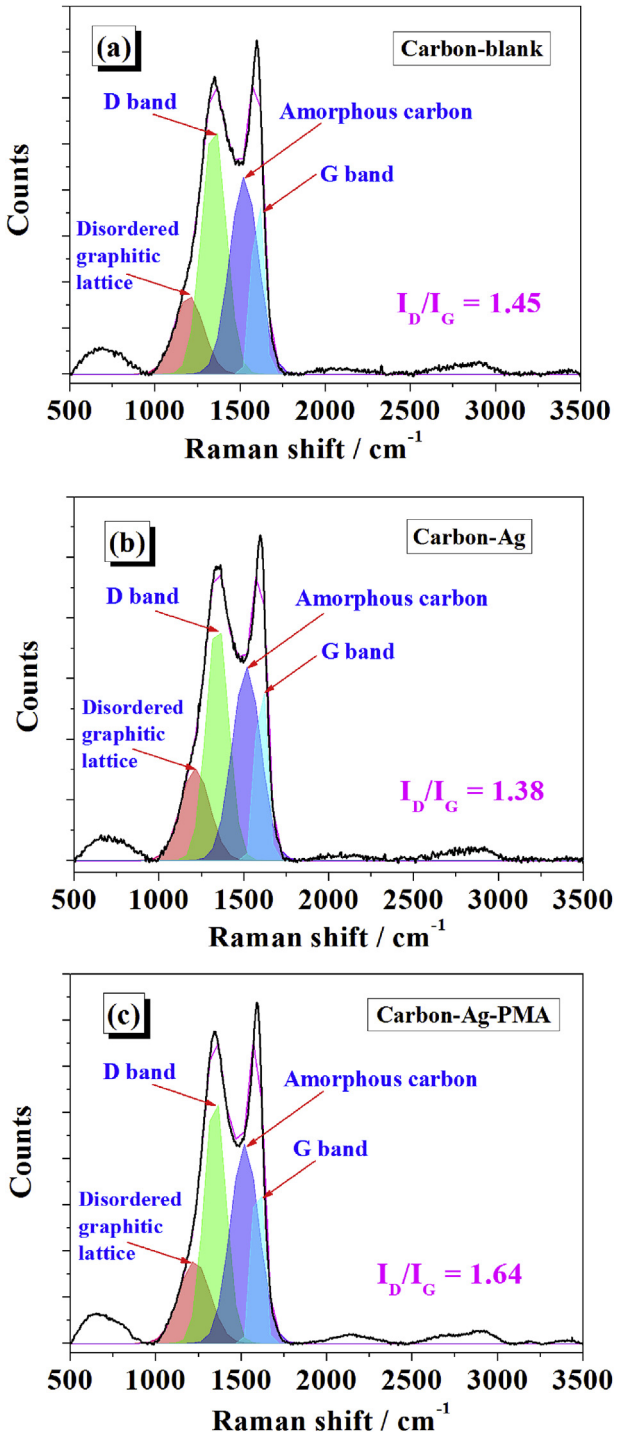

Fig. 1. Raman spectra of the ***Carbon-blank, Carbon-Ag, Carbon-Ag-PMA*** samples.

of graphitization.

For further analyze the carbon feature in a quantitative manner, we used the formula: $I_D/I_G = C_\lambda/L_a$, where I_D/I_G is the intensity of the D peak to that of the G peak, C_λ usually as 4.4 nm, and L_a denotes the graphitic in-plane microcrystallite size [34]. The I_D/I_G of the ***Carbon-blank, Carbon-Ag, Carbon-Ag-PMA*** samples are of 1.45, 1.38, and 1.64, and the resulting L_a can be calculated as 3.03, 3.19, and 2.68 nm, respectively. It is thereby inferred that the incorporation of Ag and/or PMA has to some extent exerted impacts on the carbon microstructures.

Carbon porosity is another crucial factor that quite affects the electrochemical behaviors of supercapacitors. The pristine ***Carbon-blank*** sample without further treatment exhibits type-I isotherm, as shown in Fig. 2a, typically indicating the predominant presence of micropores within carbon matrix according to the International Union of Pure and Applied Chemistry (IUPAC) classification. Moreover, this microporous nature is further evinced by the corresponding pore size distribution (PSD) result, as depicted in Fig. 2b, where the ***Carbon-blank*** sample almost entirely falls into the scope of micropores with representative peaks at 0.78, 0.97 and 1.22 nm, respectively. Accordingly, the ***Carbon-blank*** sample shows large BET surface area of 2269 $m^2 g^{-1}$, high pore volume of 0.41 $cm^3 g^{-1}$ and average pore width of 1.18 nm, as given in Table 1.

When further incorporating the ***Carbon-blank*** sample with Ag substance, the ***Carbon-Ag*** sample comes into being. However, its porosity is anticipitated to decline to a certain extent because some carbon pores probably are blocked by Ag nanoparticles. As a consequence, the volume adsorbed of the ***Carbon-Ag*** sample has decreased as shown in Fig. 2a, compared to the ***Carbon-blank*** sample. Indeed, the BET surface area of the ***Carbon-Ag*** sample has reduced to be 2087 $m^2 g^{-1}$, and pore volume to be 0.25 $cm^3 g^{-1}$, although the PSD profile has not changed dramatically (in Fig. 2b).

Yet, the ***Carbon-Ag-PMA*** sample that further adding PMA substance into the ***Carbon-Ag*** sample has achieved much lower BET surface area of 847 $m^2 g^{-1}$, and pore volume of 0.15 $cm^3 g^{-1}$, accompanying with the obvious change of PSD result, as shown in Fig. 2 and Table 1. The reason is perhaps due to the fact that PMA is more inclined to be adsorbed in microporosity as a consequence of a greater confinement in this kind of pores [16]. To all appearances, the incorporation of Ag and/or PMA has greatly modulated the porosity of the present microporous carbon materials.

The ***Carbon-blank, Carbon-Ag, Carbon-Ag-PMA*** samples were further tested by XPS technique to investigate the elemental compositions, electronic states etc. Fig. 3a displays the contrast XPS survey spectra of these samples with binding energy scoping from 0 to 1300 eV. In details, the ***Carbon-blank*** sample indicates obvious C 1s and O 1s peaks at ca. 283.5 and 533.6 eV, respectively, whilst one additional minor peak at 373.4 eV assigned to Ag 3d occurs concerning the ***Carbon-Ag*** sample. As for the ***Carbon-Ag-PMA*** sample, extra peaks indexed as P 2p and Mo 3d also emerge in its own survey spectrum.

Next, more elaborative XPS analysis of the ***Carbon-Ag-PMA*** sample was carried out. Fig. 3b reveals the core-level C 1s spectrum and four different peaks are basically deconvoluted by XPS PEAK software. They are located at ca. 284.8, 286.7, 288.5, and 291.0 eV, which are approximately vested in C–C/C=C, C–O, –COO/C=O, and π–π^*, respectively [35]. With respect to core-level Ag 3d peak, as shown in Fig. 3c, it can be fitted into two isolated peaks at 368.5 and 374.6 eV, which attribute to Ag $3d_{5/2}$ and Ag $3d_{3/2}$, respectively [36,37]. Besides, the core-level XPS spectrum of Mo 3d for the ***Carbon-Ag-PMA*** sample in Fig. 3d shows two pairs of peaks at the binding energies of 233.0 and 236.2 eV, respectively. These peaks correspond to Mo $3d_{5/2}$ and Mo $3d_{3/2}$, suggesting that molybdenum is in the VI oxidation state [21]. Regarding the core-level P 2p, it is centered at ca. 134.1 eV, primarily assignable to P–O bond [12].

In addition, the atomic contents of C, O, Ag and Mo from XPS analysis concerning the ***Carbon-blank, Carbon-Ag, Carbon-Ag-PMA*** samples are listed in Table 2. Furthermore, based on mass fraction, the contents of Ag towards the ***Carbon-Ag, Carbon-Ag-PMA*** samples are *ca.* 2.25% and 3.94%, respectively, whilst that of PMA of the ***Carbon-Ag-PMA*** sample are *ca.* 18.26%.

The intrinsic structures of the ***Carbon-blank, Carbon-Ag, Carbon-Ag-PMA*** samples were tested by techniques of HRTEM together with elemental mapping and the resulting images are vividly depicted in Fig. 4. The HRTEM images in Fig. 4 a-b have indicated the fact regarding the ***Carbon-blank*** sample that the as-received activated carbon (*abbr.* AC) materials are basically composed of irregular carbon blocks, visibly exhibiting microporous features also with low degree of graphitization. Besides, mappings of C/O elements of the ***Carbon-blank*** sample are also apparent, as displayed in Fig. 4c.

With respect to the ***Carbon-Ag*** sample, the occurrence of Ag nanoparticles (10–30 nm in sizes) coexistent with carbon materials is clearly discerned in Fig. 4 d-e. Furthermore, the HRTEM image as well elemental mapping s in Fig. 4g obviously reveal uniform distribution of C/O/Ag species has emerged. Fig. 4h shows the typical HRTEM image of Ag nanoparticle taken from the hybrid of AC/Ag, in which there exists overt fringe lattices of ~0.24 nm, primarily indexed as {111} crystal planes of Ag (JCPDS 04–0783). Besides, the existence of silver also was clarified by XRD pattern of the ***Carbon-Ag-PMA*** sample, as depicted in Fig. S1. Moreover, as for the case of ***Carbon-Ag-PMA***, the corresponding HRTEM and elemental

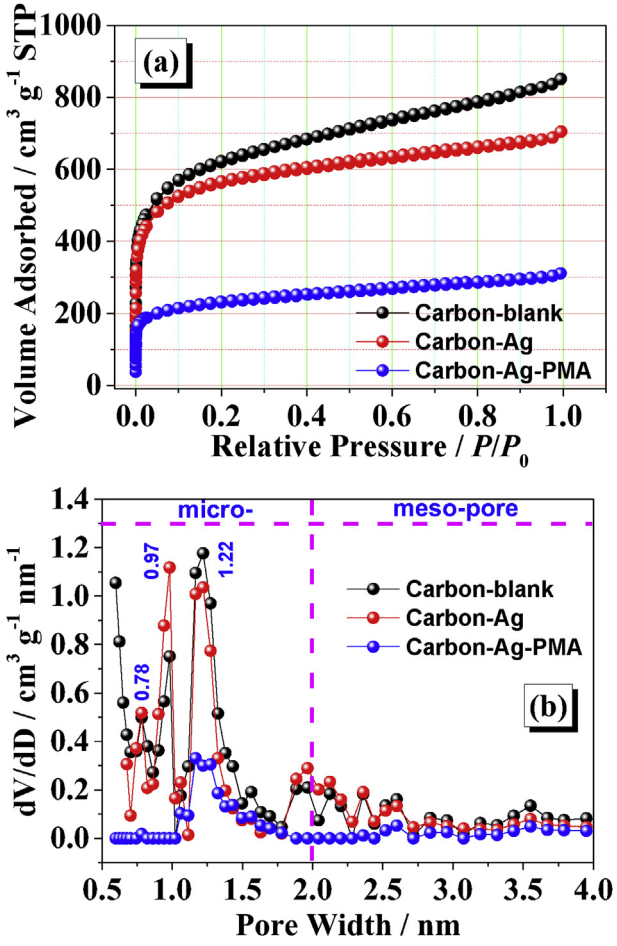

Fig. 2. The ***Carbon-blank, Carbon-Ag, Carbon-Ag-PMA*** samples: (a) N_2 adsorption-desorption isotherms; (b) Pore size distribution curves.

Table 1
Summary of the pore structures of the carbon materials.

samples	BET surface area/$m^2\ g^{-1}$	Total pore volume/$cm^3\ g^{-1}$	Pore width/nm
Carbon-blank	2269	0.41	1.18
Carbon-Ag	2087	0.25	1.17
Carbon-Ag-PMA	847	0.15	1.31

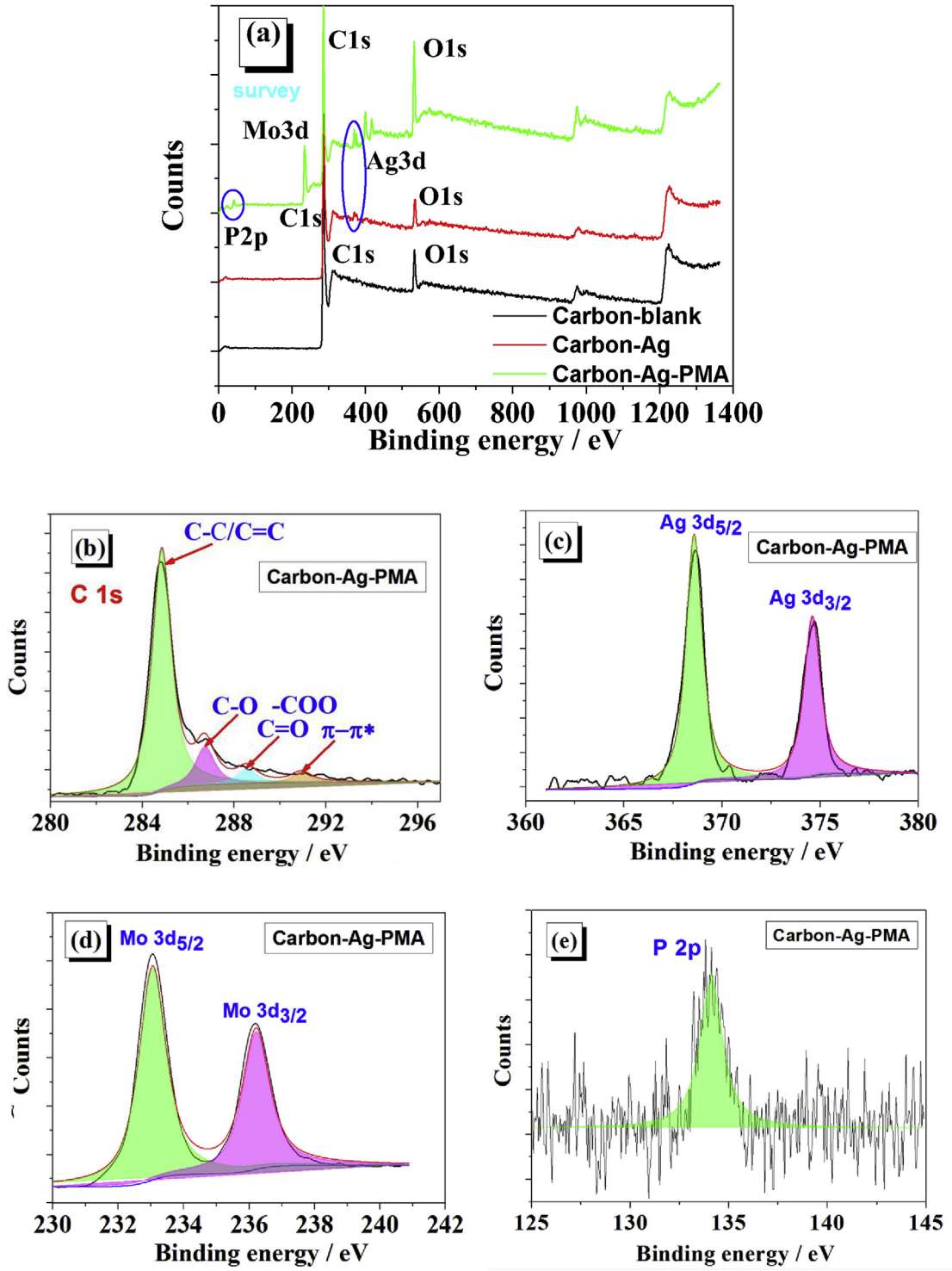

Fig. 3. The ***Carbon-blank, Carbon-Ag, Carbon-Ag-PMA*** samples: (a) Survey; as well as the ***Carbon-Ag-PMA*** sample: (b) C 1s; (c) Ag 3d; (d) Mo 3d; (e) P 2p.

Table 2
The atomic contents (%) of C, O, Ag and Mo from XPS analysis.

samples	C	O	Ag	P	Mo
Carbon-blank	93.30	6.70	/	/	/
Carbon-Ag	94.05	5.69	0.26	/	/
Carbon-Ag-PMA	89.71	6.11	0.55	1.12	2.51

adsorbed in microporosity [16]. Taking into the above consideration, schematic illustration for the structure of microporous carbon/Ag/PMA hybrid is given in Fig. 5a, including the probable avenues for electron/electrolyte ion transportations. Note that there exist abundant minor Ag nanoparticles, which makes it possible for the contact each other. And given on this kind of close

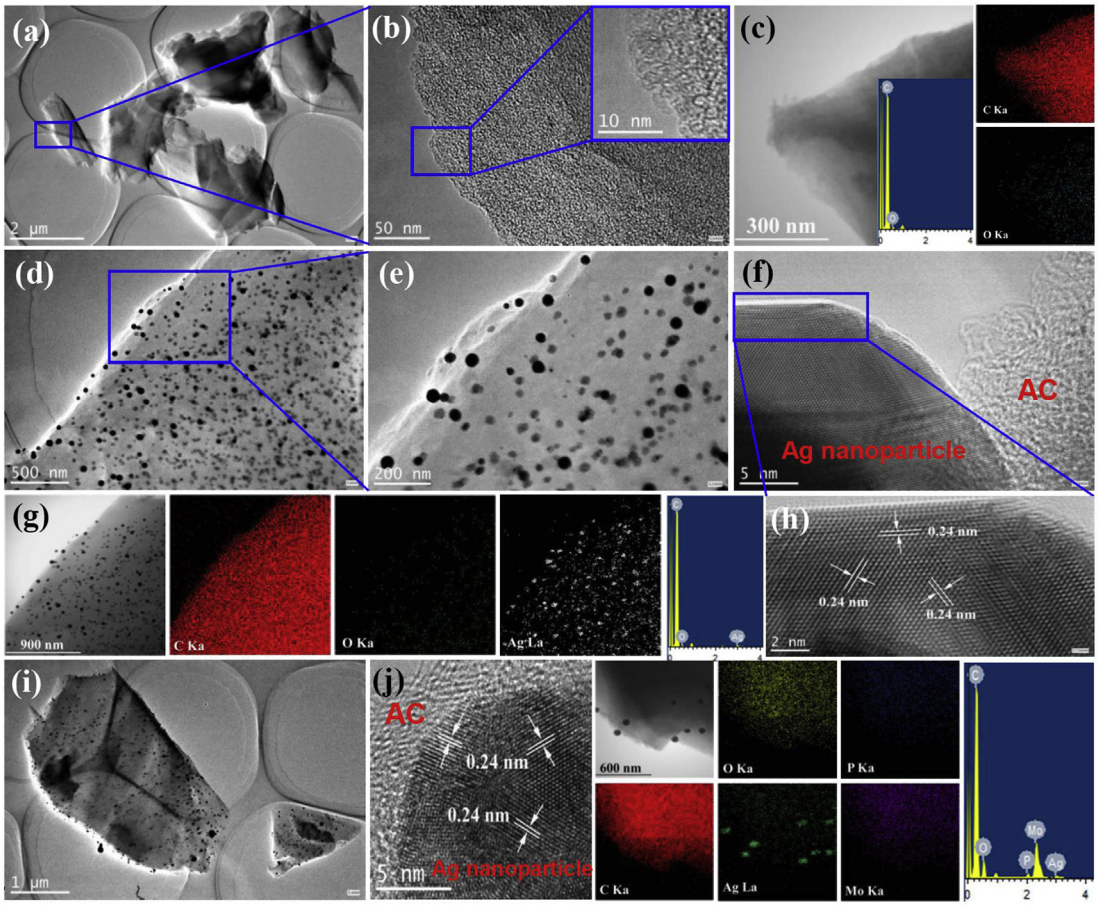

Fig. 4. HRTEM and elemental mapping images of the samples: (a–c) ***Carbon-blank;*** (d–h) ***Carbon-Ag;*** (i–j) ***Carbon-Ag-PMA***.

mappings become more interesting, as given in Fig. 4 i-j. In particular, the mappings of C/O/Ag/P/Mo have distributed very uniformly, thus strongly proving the coexistence of these elements within the ***Carbon-Ag-PMA*** sample.

3.2. Electrochemical measurements

In present work, based on Raman result shown in Fig. 1a, it is seen that the microporous carbon is in amorphous status and can contribute EDLCs as well. Therefore, to improve its electrical conductivity as well as cycling stability, certain amount of Ag substance was commonly incorporated, such as the cases of graphene/silver nanowires [9], and graphene-silver nanoparticles-polypyrrole nanocomposite [11]. On the other side, judged from Table 1, the porosity has just slightly decreased after the addition of Ag to microporous carbon materials, hence indicating that most of the as-produced present Ag nanoparticles are not located in the interior of micropores but uniformly distributed throughout the carbon matrix (as in details revealed in Fig. 4). Nevertheless, as reported before, PMA that contributes pseudo-capacitances prefers to be contacting, electronic conductivity has been improved to some extent [11]. Regarding the pseudo-capacitive PMA, its unit structure is also presented in Fig. 5b. Distinctly, this kind of ternary structure of microporous carbon/Ag/PMA hybrid could deliver superior electrochemical performance for supercapacitor applications.

Electrochemical performance of the ***Carbon-blank, Carbon-Ag, Carbon-Ag-PMA*** samples was firstly tested in a three-electrode configuration using 1 mol L^{-1} H_2SO_4 solution as aqueous electrolyte. Fig. 5a indicates the comparative CV curves at the scan rate of 20 mV s^{-1} when designating the potential window as −0.6–0.6 V. The CV profile of the ***Carbon-blank*** sample in Fig. 6a is approximate to the ellipse, to a large extent deviated from standard rectangle that usually implies the ideal EDLCs for carbon-based supercapacitors. Evidently, the amorphous nature together with surface functionalities of the ***Carbon-blank*** sample makes it far from ideal one. To largely ameliorate the pristine carbon materials, certain mass of Ag substance was incorporated, leading to the formation of the ***Carbon-Ag*** sample. As a result, the corresponding CV profile has obviously improved to be nearly rectangular in shape, as shown in Fig. 6a. And the integral CV area of the ***Carbon-Ag*** sample has also

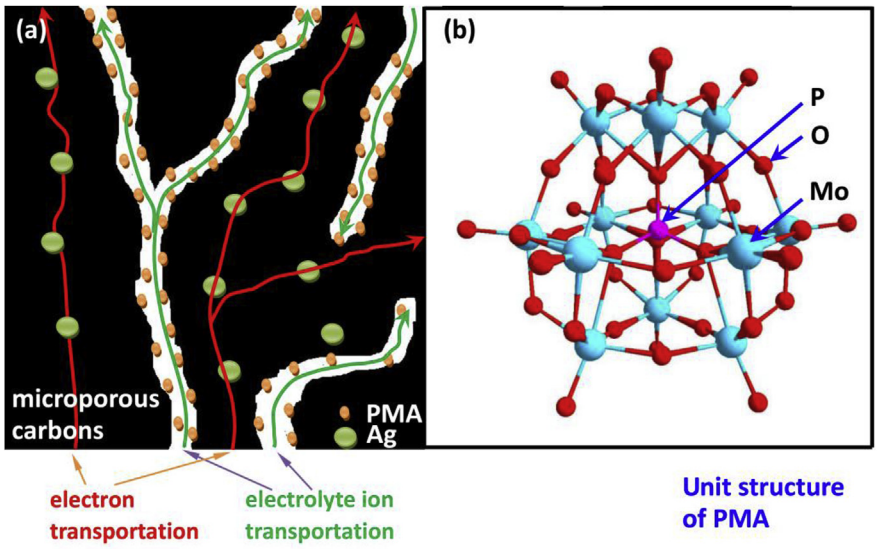

Fig. 5. (a) Schematic illustration for the structure of microporous carbon/Ag/PMA hybrid; (b) Unit structure of PMA.

enlarged than that of the ***Carbon-blank*** sample, revealing the augment of specific capacitance primarily owing to the increase of electrical conductivity [36,37]. As for the case of the ***Carbon-Ag-PMA*** sample assisted with redox active PMA, its CV profile turns to be the largest one in area, and several pairs of redox peaks also emerge in the potential range of −0.6–0.6 V, as clearly depicted in Fig. 6a. Consequently, it is inferred that, concerning the ***Carbon-Ag-PMA*** sample, although the incorporation of PMA causes the BET surface area and pore volume decreasing (commonly resulting in the drop of EDLCs), the pseudo-capacitive contribution of PMA has greatly made up for the total capacitance. That is why the ***Carbon-Ag-PMA*** sample delivers the largest CV result.

What is worth paying attention to is the redox behaviors of PMA within the hybrid of carbon/Ag/PMA in aqueous H_2SO_4 electrolyte. As well reported, PMA usually exhibits three pairs of small reversible redox peaks corresponding to the three two-electron transfer reactions of the PMo12 species under various circumstances, such as potential window of −0.3–0.8 V in 1 M H_2SO_4 or [Bmim]HSO_4 [38], potential window of −0.2–1 V in 1 M H_2SO_4 [19], potential window of −0.2–0.8 V in 1 M H_2SO_4 [18,20]. And the proposed redox reactions of PMA are given in the following equations [39]:

$$PMo_{12}O_{40}^{3-} + 2e^- + 2H^+ \leftrightarrow H_2PMo_2^{V}Mo_{10}^{VI}O_{40}^{3-} \quad (1)$$

$$H_2PMo_2^{V}Mo_{10}^{VI}O_{40}^{3-} + 2e^- + 2H^+ \leftrightarrow H_4PMo_4^{V}Mo_8^{VI}O_{40}^{3-} \quad (2)$$

$$H_4PMo_4^{V}Mo_8^{VI}O_{40}^{3-} + 2e^- + 2H^+ \leftrightarrow H_6PMo_6^{V}Mo_6^{VI}O_{40}^{3-} \quad (3)$$

Thus, the use of PMA as a redox-active component in carbon/Ag/PMA hybrid material provides not only an added faradaic contribution to the total capacitance within the electrode, but also a large potential beyond the traditional one (~1.0 V for aqueous H_2SO_4 solution) which allows an increase of the range of stability substantially with respect to the pristine activated carbon electrode.

Fig. 6b shows the contrastive GCD curves of the ***Carbon-blank, Carbon-Ag, Carbon-Ag-PMA*** samples at a charging-discharging current density of 2 A g^{-1} with a potential window of −0.6–0.6 V. From the viewpoint of outlines, the ***Carbon-blank*** sample has to large extent deviated from ideal triangle, whereas the other samples show better triangular shapes. And also the GCD tendency in Fig. 6b is almost the same as CV results in Fig. 6a. On the other hand, the IR drop at the turning point of charge-discharge indicates the energy loss due to the internal resistance [40]; the inset in Fig. 6b show that the IR drop clearly decreases by the incorporation of Ag and/or PMA, and the ***Carbon-Ag-PMA*** sample exhibits the smallest one, revealing its lowest internal resistance.

Nyquist plots of the ***Carbon-blank, Carbon-Ag, Carbon-Ag-PMA*** samples are displayed in Fig. 6c. Among these samples, the ***Carbon-Ag-PMA*** sample has the smallest equivalent series resistance (ESR), the lowest inconspicuous arc in the high frequency region together with the most vertical shape at lower frequencies, well indicating its superior capacitive behaviors such as the least electronic resistance and shortest ion diffusion etc [41]. On the contrary, the ***Carbon-blank*** sample possesses the worst Nyquist performance. Notably, it is also apparent to us that the variation tendency of Nyqusit is quite similar to the IR drops highlighted in Fig. 6b.

Fig. 6d shows the specific capacitance versus current density when tested in a three-electrode configuration. Basically, the capacitance sequence is as follows: ***Carbon-Ag-PMA*** > ***Carbon-Ag*** > ***Carbon-blank***. At a fixed current density of 1 A g^{-1}, the specific capacitances are of 113.9, 154.2, and 182.3 F g^{-1}, respectively, towards the ***Carbon-blank, Carbon-Ag, Carbon-Ag-PMA*** samples, respectively. Next, we calculated their capacitance retention (rate capability) at the current density of 10, 15 and 20 A g^{-1}, respectively, and the histogram of results is depicted in Fig. 6e. On the whole, the ***Carbon-Ag-PMA*** sample exhibits the best capacitance retention whereas the ***Carbon-blank*** sample does the worst, no matter how much the current density is.

Coulombic efficiency is another important factor with which charge (electrons) is transferred in a system facilitating an electrochemical reaction. For ideally linear galvanostatic charge/discharge (GC/GD) curves, we can directly use the charging and discharging time. But, for most of the cases, the GCD plots are nonlinear in shapes (coulombic efficiency is sometimes named with energy efficiency), and thereby it should be calculated by the integral current area under the GD and GC curves [42,43]. Coulombic efficiency of the ***Carbon-blank, Carbon-Ag, Carbon-Ag-PMA*** samples at the current density of 1 A g^{-1} are calculated to be 55.7%, 86.9% and 91.7%, respectively, as revealed in Fig. 6f. As a consequence, incorporating Ag and PMA into microporous carbon materials has indeed improved the coulombic efficiency.

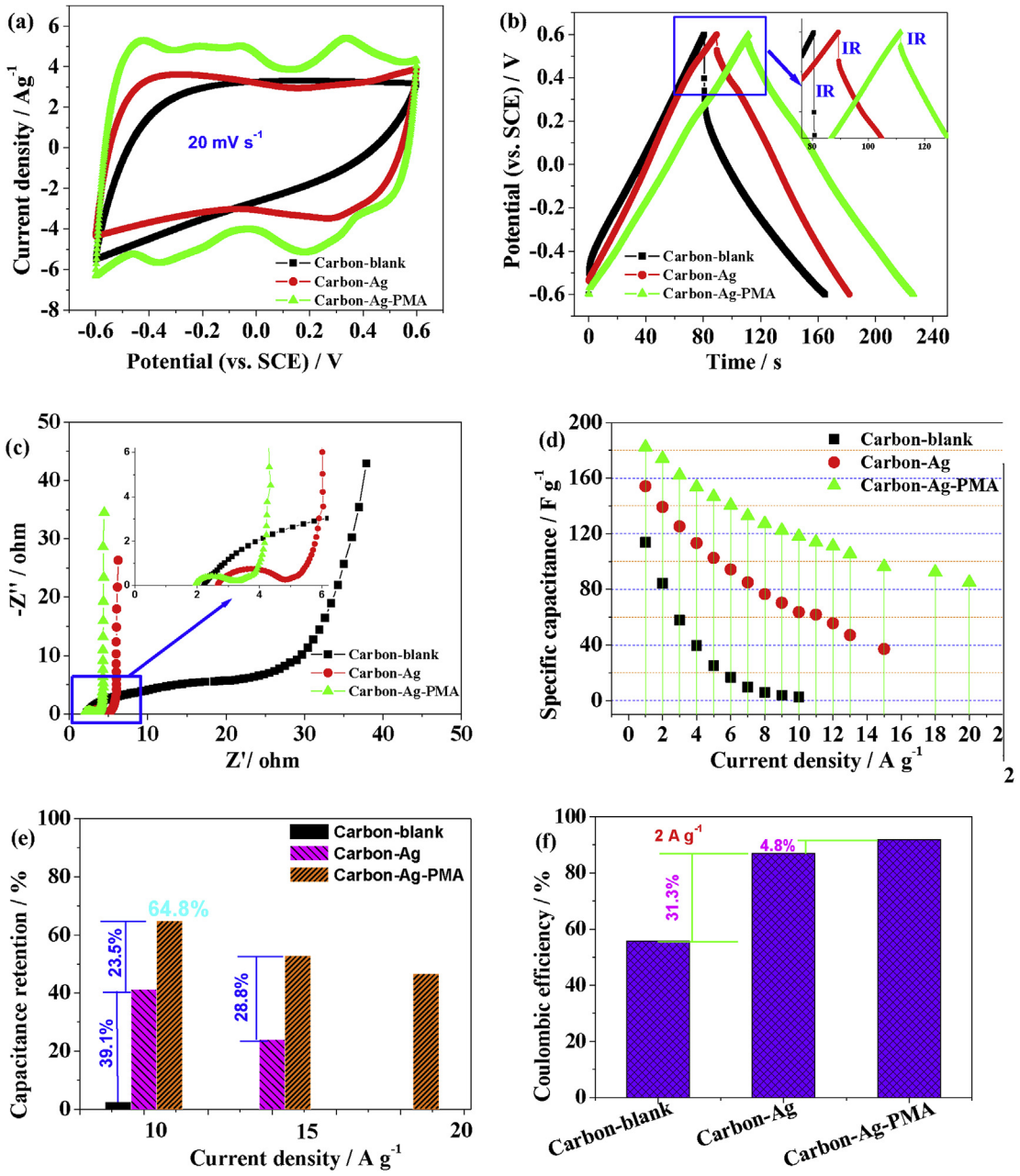

Fig. 6. Electrochemical performance of the ***Carbon-blank, Carbon-Ag, Carbon-Ag-PMA*** samples tested in a three-electrode configuration: (a) CV curves; (b) GCD curves (the inset of IR drop); (c) Nyquist plots (the inset of enlarged one); (d) Specific capacitance versus current density; (e) Capacitance retention versus current density; (f) Coulombic efficiency.

Next, a two-electrode test cell configuration was used for the ***Carbon-blank, Carbon-Ag, Carbon-Ag-PMA*** samples because it provides the most accurate measure of a material's performance for supercapacitors [44]. Fig. 7a indicates the contrast CV curves at the scan rate of 20 mV s^{-1} when fixing the potential window of 0–1.2 V. From the viewpoint of integral CV area, the sequence is as follows: ***Carbon-blank*** < ***Carbon-Ag*** < ***Carbon-Ag-PMA***, quite consistent with that measured in a three-electrode configuration (Fig. 6a). Analogously, the sequence of IR drop of GCD results in Fig. 7b is also equal to the one in Fig. 6b.

Furthermore, in terms of the calculation from GCD curves in Fig. 7b, specific capacitances versus current densities are achieved and displayed in Fig. 7c. On the whole, the ***Carbon-Ag-PMA*** sample delivers the largest specific capacitances while the ***Carbon-blank*** indicates the smallest ones. For example, the specific capacitances obtained at the current density of 1 A g^{-1} are of 63.6, 89.9, and 113.4 F g^{-1}, respectively, towards the ***Carbon-blank, Carbon-Ag, Carbon-Ag-PMA*** samples. Besides, based on the capacitance data in Fig. 7c, the capacitance retention (rate capability) versus current density is also given, as shown in Fig. 7d. It is generally revealed that incorporating Ag and/or PMA into carbon matrix has largely elevated the capacitance retention. For instance, the amplification of the ***Carbon-Ag, Carbon-Ag-PMA*** samples has reached up to 18.3% and 7.4%, respectively, when fixing the current density of 10 A g^{-1}. Moreover, what is noteworthy to us is that enhancing the current density always leads to the decrease of capacitance retention, as indicated in Figs. 6e and 7d. This point is incurred by the fact that ion diffusivity becomes a limiting factor at high current (high power) because regions where ions fail to diffuse increase, hence resulting in a decrease in capacitance [45]. With regard to

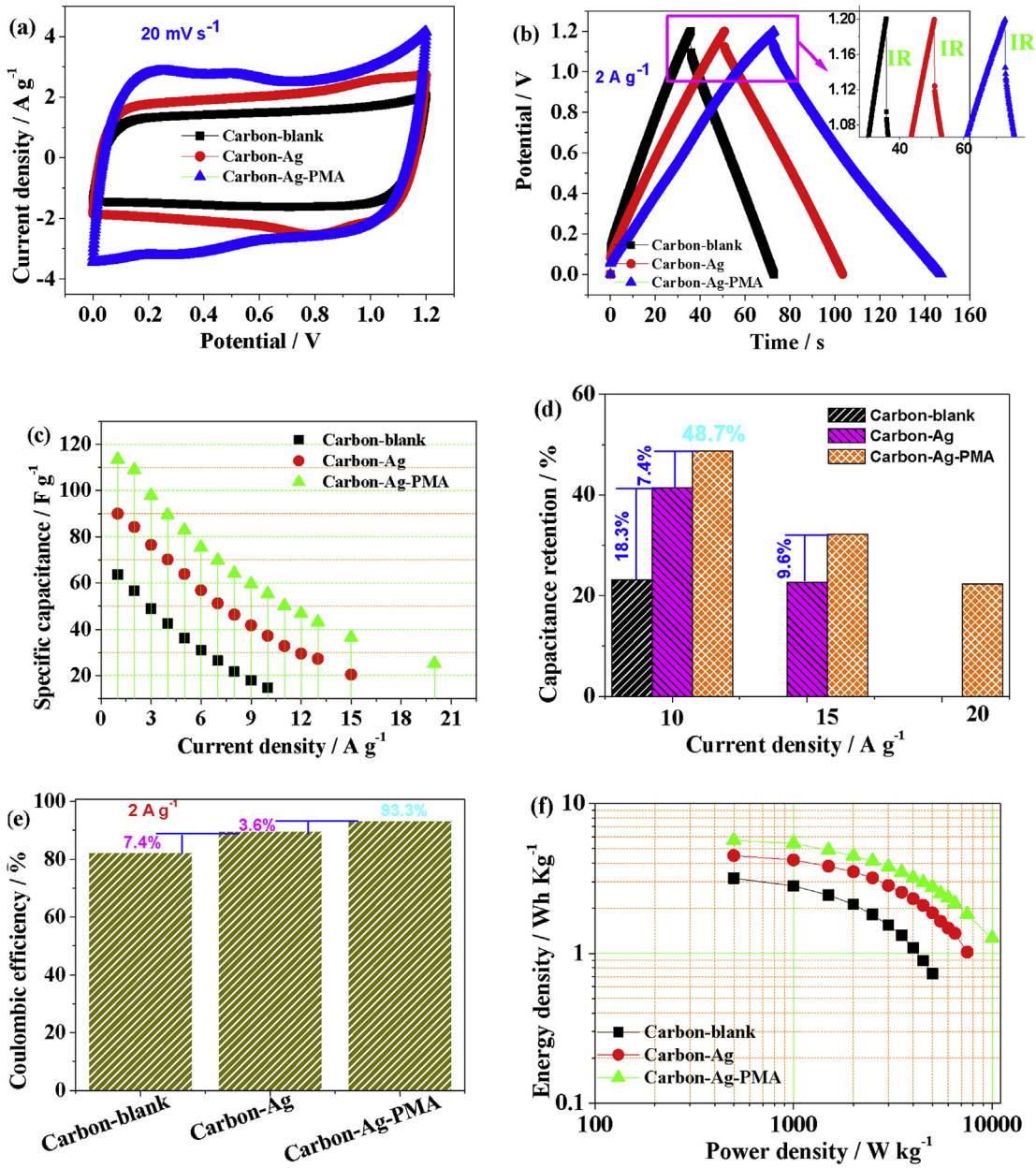

Fig. 7. Electrochemical performance of the ***Carbon-blank, Carbon-Ag, Carbon-Ag-PMA*** samples tested in a two-electrode configuration: (a) CV curves; (b) GCD curves; (c) Specific capacitance versus current density; (d) Capacitance retention versus current density; (e) Coulombic efficiency; (f) Ragone plots (energy density vs. power density).

coulombic efficiency, it also exhibits incremental trend for the ***Carbon-blank, Carbon-Ag, Carbon-Ag-PMA*** samples, as shown in Fig. 7e.

Ragone plot illustrating the function of energy density and power density has been extensively used for performance comparison of various energy-storing devices. Conceptually, energy density describes how much energy is available, while power density shows how quickly that energy can be delivered [46,47]. Fig. 7f indicates the Ragone profiles (energy density vs. power density) and the sequence of energy densities among these samples is also the same as specific capacitances. For example, the energy densities of the ***Carbon-blank, Carbon-Ag, Carbon-Ag-PMA*** samples are of 3.18, 4.50, and 5.68 Wh kg^{-1} when measured at the power density of 500 W kg^{-1}. The present ***Carbon-Ag-PMA*** sample delivers superior energy density compared with the ones reported such as Ag NWs/3D-graphene foam/OMC (energy density of 4.5 Wh kg^{-1} at a power density of 250 W kg^{-1}) [9].

In addition, specific capacitance (*Cs*) as well as the increase fold obtained in a two-electrode configuration is summarized in Table 3. As far as increase fold is concerned, the present ***Carbon-Ag-PMA*** sample exhibits superior performance of 1.91, which is much larger than most of the reported ones, primarily owing to the present synergistic effect of Ag (increasing electronic conductivity) and PMA (increasing pseudo-capacitive contribution).

In a two-electrode configuration, the ***Carbon-blank, Carbon-Ag, Carbon-Ag-PMA*** samples were tested concerning the cycling stability that also are crucial issue for supercapacitor application. As indicated in Fig. 8a, their capacitances remain up to ca. 89.14%, 94.06% and 76.62%, respectively, within 5000 charging-discharging times. Clearly, the incorporation of Ag into pristine microporous carbon material has to some extent elevated the cycling stability owing to the enhancement of electrical conductivity; however,

Table 3
Specific capacitance (Cs) as well as the increase fold obtained in a two-electrode configuration.

Electrode material	Electrolyte	Redox additive	Current density	Cs before addition	Cs after addition	Increase fold	Ref.
AC	1 M H_2SO_4	PMA	6 mA cm^{-2}	225 mF cm^{-2}	293 mF cm^{-2}	1.30	13
SWCNT	1 M H_2SO_4	TBA-PV2Mo10	1 mA cm^{-2}	151 mF cm^{-2}	224 mF cm^{-2}	1.48	14
graphene	1 M H_2SO_4	PMA	1 A g^{-1}	95 F g^{-1}	123 F g^{-1}	1.30	15
AC	1 M H_2SO_4	PMA	2 A g^{-1}	35 F g^{-1}	45 F g^{-1}	1.29	16
AC	1 M H_2SO_4	PTA	2 mV s^{-1}	185 F g^{-1}	254 F g^{-1}	1.37	20
AC	1 M [Bmim]HSO_4	PMA	1 mV s^{-1}	126 F g^{-1}	223 F g^{-1}	1.76	38
AC	1 M H_2SO_4	PMA	1 A g^{-1}	63 F g^{-1}	114 F g^{-1}	1.91	Present work

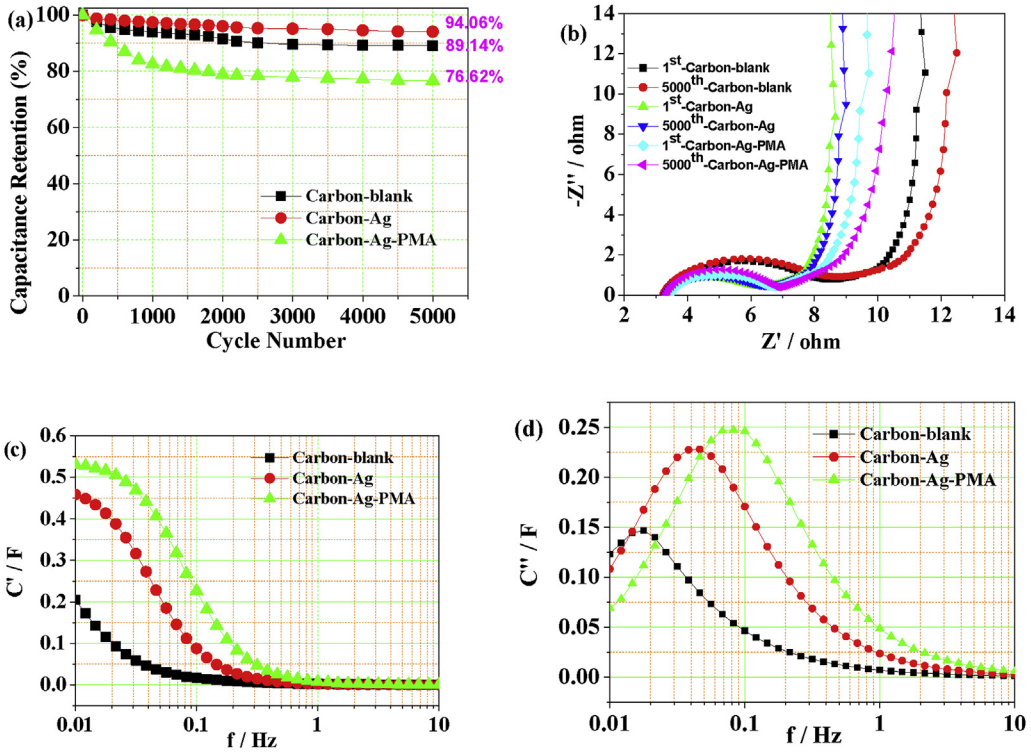

Fig. 8. The ***Carbon-blank, Carbon-Ag, Carbon-Ag-PMA*** samples tested in a two-electrode configuration: (a) Cycling stabilities within 5000 times; (b) Nyquist plots of the 1st and 5000th cycles; and evolution of (c) real and (d) imaginary part of capacitance versus frequency.

further adding PMA leads to the decrease of cycling stability primarily due to the irreversibility/instability of PMA itself.

Fig. 8b demonstrates the typical Nyquist plots of the 1st and 5000th cycle regarding the ***Carbon-blank, Carbon-Ag, Carbon-Ag-PMA*** samples. From the inconspicuous arc in the high frequency region as well as the vertical shape at low frequency, the ***Carbon-Ag, Carbon-Ag-PMA*** samples exhibit better Nyquist behaviors compared with the pristine ***Carbon-blank*** sample. In addition, Fig. 8c and d reveals the evolution of real and imaginary part of capacitance versus frequency, respectively. In Fig. 8c, the real part of the complex capacitance (C') depends on the electrode structure and electrode/electrolyte interface. And the sequence of C' is as follows: ***Carbon-Ag-PMA*** > ***Carbon-Ag*** > ***Carbon-blank***.

As for imaginary part, as indicated in Fig. 8d, the capacitance C'' as a function of frequency corresponds to the dielectric loss of the electrolyte occurring during rotation or movement of the molecules of solid electrolyte [48]. Typically, the three profiles go through a maximum at a particular frequency f_0. This frequency represent the dielectric relaxation time by the equation $t_0 = 1/f_0$, revealing the time taken by the supercapacitor to reach half of the low frequency capacitance [49]. Here, the f_0 data for the ***Carbon-blank, Carbon-Ag, Carbon-Ag-PMA*** samples are of 0.017, 0.044, and 0.084 Hz, hence resulting in t_0 data of 58.82, 22.73, and 11.90 s, respectively, basically complying with the Nyquist results in Fig. 8c.

4. Conclusions

In summary, a new energy system of microporous carbon/Ag/PMA as efficient electrode hybrid material has been developed for supercapacitors, which leads to the contribution of EDLCs, electrical conductivity and pseudocapacitance, respectively.

The dual incorporation of Ag and PMA into microporous carbon materials has largely modulated the pore structures as well as the resulting capacitive behaviors, including the decrease of surface area and pore volume, and the enhancement of specific capacitance, rate capability and coulombic efficiency but drop of cycling stability.

For the microporous carbon/Ag/PMA electrode hybrid material, it produces large energy density of 5.68 Wh kg^{-1} at the power density of 500 W kg^{-1}, which is almost 1.80 fold of pristine microporous carbon. It is bright spot, beyond most of the scientific reports.

The present hybridization of polyoxometalate, carbon materials as well as conducting agent could be easily extended to other

substances, providing an alternative electrode material for high performance supercapacitors.

Acknowledgments

This work was financially supported by National Natural Science Foundation of China (51602003, 11704376), Startup Foundation for Doctors of Anhui University (J01003211), and Key Research and Development Projects of Anhui in 2018 (1804a09020064).

Appendix A. Supplementary data

Supplementary data to this article can be found online at https://doi.org/10.1016/j.jallcom.2019.03.374.

References

[1] L.L. Zhang, X.S. Zhao, Carbon-based materials as supercapacitor electrodes, Chem. Soc. Rev. 38 (2009) 2520–2531.
[2] Y. Zhai, Y. Dou, D. Zhao, P.F. Fulvio, R.T. Mayes, S. Dai, Carbon materials for chemical capacitive energy storage, Adv. Mater. 23 (2011) 4828–4850.
[3] J. Wei, Z. Zang, Y. Zhang, M. Wang, J. Du, X. Tang, Enhanced performance of light-controlled conductive switching in hybrid cuprous oxide/reduced graphene oxide (Cu_2O/rGO) nanocomposites, Optic Lett. 42 (2017) 911–914.
[4] Z. Zang, X. Zeng, M. Wang, W. Hu, C. Liu, X. Tang, Tunable photoluminescence of water-soluble AgInZnS–graphene oxide (GO) nanocomposites and their application in-vivo bioimaging, Sensor. Actuator. B 252 (2017) 1179–1186.
[5] P. Simon, Y. Gogotsi, Materials for electrochemical capacitors, Nat. Mater. 7 (2008) 845–854.
[6] M.F. El-Kady, V. Strong, S. Dubin, R.B. Kaner, Laser scribing of high-performance and flexible graphene-based electrochemical capacitors, Science 335 (2012) 1326–1330.
[7] E. Frackowiak, F. Béguin, Carbon materials for the electrochemical storage of energy in capacitors, Carbon 39 (2001) 937–950.
[8] M. Sawangphruk, M. Suksomboon, et al., High-performance supercapacitors based on silver nanoparticle–polyaniline–graphene nanocomposites coated on flexible carbon fiber paper, J. Mater. Chem. A 1 (2013) 9630–9636.
[9] T. Zhi, W. Zhao, X. Liu, A. Chen, Z. Liu, F. Huang, Highly conductive ordered mesoporous carbon based electrodes decorated by 3D graphene and 1D silver nanowire for flexible supercapacitor, Adv. Funct. Mater. 24 (2014) 2013–2016.
[10] L. Sun, L. Du, S. Tan, Z. Zang, C. Zhao, W. Mai, Flexible electrochromic supercapacitor hybrid electrodes based on tungsten oxide films and silver nanowires, Chem. Commun. 52 (2016) 6296–6299.
[11] P.K. Kalambate, R.A. Dar, S.P. Karna, A.K. Srivastava, High performance supercapacitor based on graphene-silver nanoparticles-polypyrrole nanocomposite coated on glassy carbon electrode, J. Power Sources 276 (2015) 262–270.
[12] Z.J. Zhang, Q.C. Zheng, L. Sun, D. Xu, X.Y. Chen, Two-dimensional carbon nanosheets for high-performance supercapacitors: large-scale synthesis and codoping with nitrogen and phosphorus, Ind. Eng. Chem. Res. 56 (2017) 12344–12353.
[13] D. Xu, W. Hu, X.N. Sun, P. Cui, X.Y. Chen, Redox additives of Na_2MoO_4 and KI: synergistic effect and the improved capacitive performances for carbon-based supercapacitors, J. Power Sources 341 (2017) 448–456.
[14] D. Xu, X.N. Sun, W. Hu, X.Y. Chen, Carbon nanosheets-based supercapacitors: design of dual redox additives of 1, 4-dihydroxyanthraquinone and hydroquinone for improved performance, J. Power Sources 357 (2017) 107–116.
[15] M. Genovese, K. Lian, Polyoxometalate modified inorganic-organic nanocomposite materials for energy storage applications: a review, Curr. Opin. Solid State Mater. Sci. 19 (2015) 126–137.
[16] P. Palomino, J. Suarez-Guevara, et al., Influence of texture in hybrid carbon-phosphomolybdic acid materials on their performance as electrodes in supercapacitors, Carbon 111 (2017) 74–82.
[17] H.Y. Chen, R. Al-Oweini, J. Friedl, C.Y. Lee, L. Li, U. Kortz, U. Stimming, M. Srinivasan, A novel SWCNT-polyoxometalate nanohybrid material as an electrode for electrochemical supercapacitors, Nanoscale 7 (2015) 7934–7941.
[18] J. Suarez-Guevara, V. Ruiz, P. Gomez-Romero, Stable graphene–polyoxometalate nanomaterials for application in hybrid supercapacitors, Phys. Chem. Chem. Phys. 16 (2014) 20411–20414.
[19] V. Ruiz, J. Suarez-Guevara, P. Gomez-Romero, Hybrid electrodes based on polyoxometalate-carbon materials for electrochemical supercapacitors, Electrochem. Commun. 24 (2012) 35–38.
[20] M. Genovese, K. Lian, Polyoxometalate modified pine cone biochar carbon for supercapacitor electrodes, J. Mater. Chem. A 5 (2017) 3939–3947.
[21] D.P. Dubal, N.R. Chodankar, A. Vinu, D.H. Kim, P. Gomez-Romero, Asymmetric supercapacitors based on reduced graphene oxide with different polyoxometalates as positive and negative electrodes, ChemSusChem 10 (2017) 2742–2750.
[22] P. Palomino, J. Suarez-Guevara, et al., Influence of texture in hybrid carbon-phosphomolybdic acid materials on their performance as electrodes in supercapacitors, Carbon 111 (2017) 74–82.
[23] J. Suarez-Guevara, V. Ruiz, P. Gomez-Romero, Hybrid energy storage: high voltage aqueous supercapacitors based on activated carbon-phosphotungstate hybrid materials, J. Mater. Chem. A 2 (2014) 1014–1021.
[24] Y.H. Ding, J. Peng, H.Y. Lu, Y. Yuan, S.U. Khan, Tungsten addenda mixed heteropolymolybdates supported on functionalized graphene for high performance aqueous supercapacitors, RSC Adv. 6 (2016) 81085–81091.
[25] M. Genovese, Y.W. Foong, K. Lian, The unique properties of aqueous polyoxometalate (POM) mixtures and their role in the design of molecular coatings for electrochemical energy storage, Electrochim. Acta 199 (2016) 261–269.
[26] Y. Zhang, S.J. Park, Incorporation of RuO_2 into charcoal-derived carbon with controllable microporosity by CO_2 activation for high-performance supercapacitor, Carbon 122 (2017) 287–297.
[27] Y. Zhang, S.J. Park, Au–pd bimetallic alloy nanoparticle-decorated $BiPO_4$ nanorods for enhanced photocatalytic oxidation of trichloroethylene, J. Catal. 355 (2017) 1–10.
[28] Y. Zhang, S.J. Park, Bimetallic AuPd alloy nanoparticles deposited on MoO_3 nanowires for enhanced visible-light driven trichloroethylene degradation, J. Catal. 361 (2018) 238–247.
[29] Y. Zhang, S.J. Park, Facile construction of MoO_3@ZIF-8 core-shell nanorods for efficient photoreduction of aqueous Cr (VI), Appl. Catal. B Environ. 240 (2019) 92–101.
[30] Y. Zhang, S.J. Park, Formation of hollow MoO_3/SnS_2 heterostructured nanotubes for efficient light-driven hydrogen peroxide production, J. Mater. Chem. A 6 (2018) 20304–20312.
[31] P. Garrigue, A. Kuhn, et al., Top–down approach for the preparation of colloidal carbon nanoparticles, Chem. Mater. 16 (2004) 2984–2986.
[32] Z. Li, J. Chen, D. Pan, W. Tao, L. Nie, S. Yao, A sensitive amperometric bromate sensor based on multi-walled carbon nanotubes/phosphomolybdic acid composite film, Electrochim. Acta 51 (2006) 4255–4261.
[33] A. Sadezky, H. Muckenhuber, H. Grothe, R. Niessner, U. Pöschil, Raman microspectroscopy of soot and related carbonaceous materials: spectral analysis and structural information, Carbon 43 (2005) 1731–1742.
[34] P.K. Chu, L. Li, Characterization of amorphous and nanocrystalline carbon films, Mater. Chem. Phys. 96 (2006) 253–277.
[35] T.I.T. Okpalugo, P. Papakonstantinou, H. Murphy, J. McLanghlin, N.M.D. Brown, High resolution XPS characterization of chemical functionalized MWCNTs and SWCNTs, Carbon 43 (2005) 153–161.
[36] Z.J. Zhang, Q.C. Zheng, L. Sun, Synthesis of 2-D nanostructured $BiVO_4$:Ag hybrid as an efficient electrode material for supercapacitors, Ceram. Int. 43 (2017) 16217–16224.
[37] Z.J. Zhang, Q. Wang, Y.Q. Zhu, X.Y. Chen, Nanoporous graphitic carbon materials: systematic incorporation of p-/m-/o-nitroaniline as effective redox additives for largely improving the capacitive performance, Carbon 100 (2016) 564–577.
[38] C. Hu, E. Zhao, N. Nitta, A. Magasinski, G. Berdichevsky, G. Yushin, Aqueous solutions of acidic ionic liquids for enhanced stability of polyoxometalate-carbon supercapacitor electrodes, J. Power Sources 326 (2016) 569–574.
[39] M. Sadakane, E. Steckhan, Electrochemical properties of polyoxometalates as electrocatalysts, Chem. Rev. 98 (1998) 219–237.
[40] Q. Wu, Y. Xu, Z. Yao, A. Liu, G. Shi, Supercapacitors based on flexible graphene/polyaniline nanofiber composite films, ACS Nano 4 (2010) 1963–1970.
[41] Y. Wang, C. Wang, Y. Chen, Supercapacitor devices based on graphene materials, J. Phys. Chem. C 113 (2009) 13103–13107.
[42] A. Laheäär, P. Przygocki, Q. Abbas, F. Béguin, Appropriate methods for evaluating the efficiency and capacitive behavior of different types of supercapacitors, Electrochem. Commun. 60 (2015) 21–25.
[43] X. Huang, Q. Wang, X.Y. Chen, Z.J. Zhang, The effects of amine/nitro/hydroxyl groups on the benzene rings of redox additives on the electrochemical performance of carbon-based supercapacitors, Phys. Chem. Chem. Phys. 18 (2016) 10438–10452.
[44] V. Khomenko, E. Frackowiak, F. Béguin, Determination of the specific capacitance of conducting polymer/nanotubes composite electrodes using different cell configurations, Electrochim. Acta 50 (2005) 2499–2506.
[45] D. Futaba, K. Hata, et al., Shape-engineerable and highly densely packed single-walled carbon nanotubes and their application as super-capacitor electrodes, Nat. Mater. 5 (2006) 987–994.
[46] Z. Qiu, Y. Wang, J. Zhou, et al., Biochar-based carbons with hierarchical micro-meso-macro porosity for high rate and long cycle life supercapacitors, J. Power Sources 376 (2018) 82–90.
[47] Q. Meng, K. Qin, L. Ma, N. Zhao, et al., N-Doped porous carbon nanofibers/porous silver network hybrid for high-rate supercapacitor electrode, ACS Appl. Mater. Interfaces 9 (2017) 30832–30839.
[48] P.L. Taberna, P. Simon, J.F. Fauvarque, Electrochemical characteristics and impedance spectroscopy studies of carbon-carbon supercapacitors, J. Electrochem. Soc. 150 (2003) A292–A300.
[49] P. Sivaraman, A.B. Samui, et al., All solid supercapacitor based on polyaniline and crosslinked sulfonated poly[ether ether ketone], Electrochim. Acta 55 (2010) 2451–2456.